1

Dual-Frequency High Electric Field Generator for MRI Safety Testing of Passive Implantable Medical Devices

Shuo Song, Jianfeng Zheng, *Member, IEEE*, Yu Wang, Qingyan Wang, Wolfgang Kainz, *Member, IEEE*, Stuart A. Long, *Life Fellow*, IEEE, and Ji Chen, *Senior Member, IEEE*

Abstract-In this paper, an electric (E) field generator is developed to generate uniform and high strength E-fields at multiple frequencies. The system can be used to assess radio frequency (RF) hazards of implantable medical devices (IMDs) in magnetic resonance imaging (MRI) environments. The novel system consists of three parts, (i) a signal generating and amplifying block, (ii) a four-channel feeding network, and (iii) a rectangular resonator box. Mixed modes are utilized to generate locally uniform E-fields inside the rectangular resonator at both 64 MHz and 128 MHz, respectively. RF-induced heating for two passive IMD families are evaluated using both numerical and experimental methods inside the E-field generator. These results are compared with those obtained from standard ASTM phantom testing. The results show that the novel E-field generator is capable of evaluating RF-induced heating for passive IMDs similar to that of the ASTM phantom. Furthermore, it integrates both 1.5T and 3T RF-induced heating tests in a single system. It is much simpler compared to the ASTM test method which needs the RF coil as a source. Consequently, this small and efficient Efield generator can be used as an alternative system for RFinduced heating tests of passive IMDs in the MRI environment.

Index Terms—Cavity model, field generator design, implantable medical device (IMD), magnetic resonance imaging (MRI)

I. INTRODUCTION

AGNETIC resonance imaging (MRI) is a widely used imaging method due to its non-invasive nature and high image quality. During the MRI procedure, radio frequency (RF) signals penetrate the human body and interact with the tissues [1]-[2]. For patients with electrically conductive implantable medical devices (IMDs), the conductive parts will interact strongly with the electromagnetic (EM) fields and lead to localized RF energy deposition in tissues near the IMDs. There are numerous reports about patient burn incidents and influences on IMDs function caused by such highly concentrated power deposition [3]-[7]. Although direct in-vivo

Shuo Song, Jianfeng Zheng, Wang Yu, Qingyan Wang, Stuart A. Long and Ji Chen are with the Department of Electrical and Computer Engineering, University of Houston, TX 77204-4005 USA (e-mail: ssong11@uh.edu; jzheng4@central.uh.edu; ywang129@uh.edu; qwang25@uh.edu; long@central.uh.edu; jchen23@central.uh.edu)

W. Kainz is with the Center for Devices and Radiological Health, Food and Drug Administration, Silver Spring, MD 20852 USA (e-mail: wolfgang.kainz@fda.hhs.gov).

MRI RF-induced heating measurement methods can potentially be used for safety assessment [8]-[9], in-vitro investigation of RF-induced heating and design optimization are still needed before the IMDs can be implanted as an MR Conditional device. Such MR Conditional devices allow the patient to safely undergo an MRI scan under very specific conditions. In many cases, the in-vitro measured heating data are directly used to label an IMD MR Conditional [10][11].

Currently, performing RF-induced heating tests based on the ASTM standard requires a large sized RF coil for each frequency to be studied and a high power supply system together with a large shielded room. Such RF coils are available as part of MRI systems or equivalent test systems based on birdcage coils or TEM coils [12]-[13]. Due to potential differences in coil types and coil sizes, local incident field calibration is required [14]. Additionally, the linear variation of the E-field along the radial direction inside the ASTM phantom in a typical RF birdcage coil will limit the test region to achieve a high signal to noise ratio. The limited test region also requires accurate IMDs positioning systems to reduce experimental uncertainty [15].

Due to these limitations and with "new knowledge about RF-induced heating related to the presence of an implant in a patient undergoing an MRI examination", the new American Society of Testing and Materials (ASTM) F2182-19e² focusing on local exposure was developed [14]. In the new $19e^2$ standard, is "focusing the analysis on local exposure, rather than whole-phantom calorimetry" [16]-[19]. The in-vitro test is aimed to characterize the heating behavior of the IMD family "under the well-characterized incident field", find the possible worst-case conditions, and then reasonably infer, or numerically predict, the RF-induced heating in actual in-vivo scenarios when an IMD is implanted inside a human body [14]. Furthermore, "The phantom geometry has been further simplified and provided only as a possible example, allowing other geometries as well" [14]. All these indicates that if one can develop a test system with well-characterized local exposure, it can also be used to assess the RF-induced heating for IMDs.

Since the test locations recommended in the ASTM standard suggests that the E-fields generated by the RF coil is mainly aligned with the bore direction, typically indicated as z-direction, the quantitative heating measurements essentially capture the interaction of the IMD with E-fields in this

direction [20]-[23]. Therefore, efficient in-vitro assessment of RF-induced heating requires a strong local E-field and a well-characterized background heating.

Various types of field generating equipment has been developed for, e.g., (i) electromagnetic compatibility (EMC) tests for active IMDs, (ii) open area test of electrically powered medical devices, and (iii) immunity testing of medical devices using wireless communications. A transmission line system (TLS) is recommended in the ISO 11451-2 standard [24]. This TLS uses terminated transmission line elements to generate EM fields between the conductors and the shielded structures. However, the system requires a large chamber; additionally, the radiated fields have the risk of coupling with the chamber enclosure [25]. Another TLS based design has been proposed by McLean [26] to generate high-intensity EM fields over a wide frequency range, but the strength of the generated field changes dramatically in the test region. Groh et al. [27] reviewed other transmission line-based designs and suggested that open Transverse Electromagnetic (TEM) lines, like parallel plate guides, are faced with problems of radiation and coupling with the shielded room, while enclosed TEM lines, which have a closed structure and inside radiating elements, will make the experiments complex. The gigahertz TEM cell is also widely used in EMC tests, however, the variation of the field strength will be too large to perform stable heating measurements for IMDs [28]. For medical devices the ISO-10974 standard proposes a trough line resonator design. This device is designed to generate ultra-high fields for testing electrically short IMDs. However, the enclosed resonator structure requires a fixed length at the desired frequency, making it not suitable for a multi-frequency capable system. Other antenna-based designs, including Bilog antennas, are able to generate a strong uniform fields, but have the disadvantage of low power efficiency and require large chambers for operation [29].

In this paper we design, built, calibrate, test, and compare to the ASTM F2182 test method, a novel dual-frequency uniform E-field generator for 64MHz and 128MHz. For practical considerations, a high strength uniform E-field constrained to the inside of a rectangular box is desirable. The EM field in such a resonance structure can be characterized by transverse electric (TE) modes based on the cavity model [30].

In the proposed design, mixed TE modes of the rectangular resonator are used to generate a uniform E-field at 64 MHz and 128 MHz. The dimensions of the E-field generator are chosen as a tradeoff between (i) field homogeneity for dual-frequency capability, (ii) power efficiency, and (iii) sufficient space to test typical IMDs. The dual-frequency-in-one design requires lumped elements circuits to match the resonator at varying frequencies. Compared to the ASTM standard test system, using the ASTM phantom driven by an RF coil, the new design has the advantage of low cost, less sensitivity to IMD positioning error, ease of fabrication and operation, and most importantly, integration of both 1.5T and 3T RF-induced heating tests into one single system.

The remainder of the paper is organized as follows: Section II presents the design and development of the novel E-field generator, including (i) numerical simulations, (ii) experimental

validation, and (iii) system calibration at 64MHz and 128MHz. Section III provides numerical simulation results of the RF-induced heating for two IMD families and positioning error analysis on a selection of IMDs. RF-induced heating measurements on a selection of IMDs were performed in the E-field generator and the ASTM phantom and compared to each other in Section IV. Section V provides the discussion and section VI presents the conclusions.

II. MULTI-FREQUENCY E-FIELD GENERATOR

In this section, we describe the development of the multifrequency E-field generator system. It is followed by the calibration procedures which include both total input power calibration and local 10 cm titanium calibration procedure. The validation of the incident field generated by the system is then presented.

A. Design of the Multi-frequency E-field generator

There are several key requirements that need to be met to accomplish reliable and efficient measurements. 1) to meet the ASTM RF-induced heating test requirements, the E-field generator needs to generate a sufficiently high E-field along the longitudinal direction of the transverse plane (z-direction) similar to that at the test location inside the ASTM phantom; 2) generate a uniform E-field to minimize the positioning error, 3) be accessible from the top so that the test devices can be accurately positioned and inspected, and 4) be large enough to accommodate IMDs of typical sizes used in clinical settings.

A rectangular shaped box, shown in Fig. 1, was developed for this study. The central region of this box is then filled with gelled saline. As prescribed in the ASTM standard, the gelled saline should have a relative permittivity of 78 and an electrical conductivity of 0.47 S/m. The corresponding wavelengths for 1.5T and 3T systems are around 45 cm and 22 cm, respectively. By attaching copper-clad, flexible circuit boards with excitations to the sidewalls of the box, a cavity can be formed if appropriate cavity modes treat the top/bottom surfaces as perfect magnetic conductors. The top side of the gel box is open. To generate a uniform E-field along one direction of the transverse plane (x-z plane), the TE₁₀ mode is utilized for 64 MHz. The dimension of 300 mm by 300 mm is chosen along the x- and z-directions so that the resonance frequency of the TE₁₀ mode is around 64 MHz and there will be enough space to place typical IMDs. As the frequency of the 3T MRI increases to 128 MHz, high order modes, such as the TE₂₀ and TE₁₂ modes will have noticeable strength.

To minimize the influence of these high order modes, several methods are used. First, the dimensions of 300 mm by 300 mm are chosen to suppress the higher modes, and second, a special 4-way feeding network is developed. Four gaps are cut on the left and right walls near the four corners of the box. SMA connectors are connected to the gaps to form even and differential excitations between the front (+z) and back (-z) box walls, as shown in Fig. 1. Two gaps on the cavity's front and back walls are cut for decoupling the left (-x) and right (+x) channels. Such a feeding network ensures that only modes with

major E-field components along the z-direction can be excited and the E-field of those modes will be symmetric with respect to both the x-axis and z-axis.

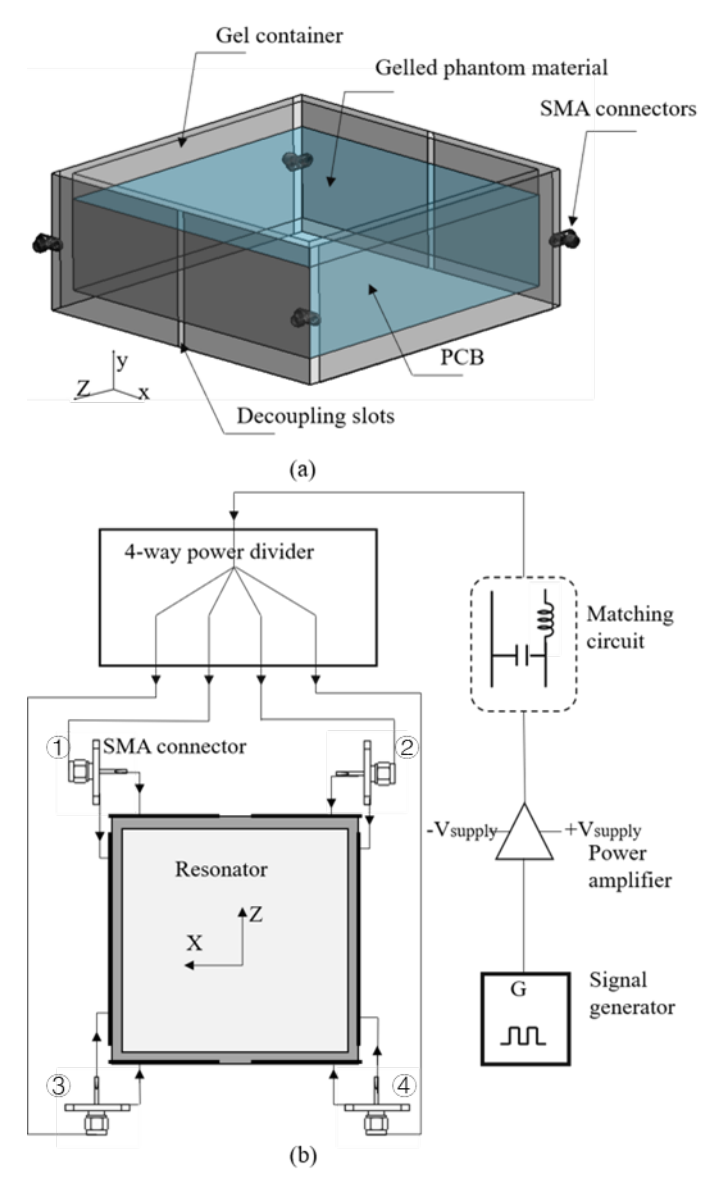


Fig. 1. (a): E-field generator design, (b): system illustration.

Fig. 1 (b) illustrates the schematic of the system. The signal from a signal generator is amplified using a power amplifier (ZHL-100W-52-S+ from Mini-Circuits) supplied with a direct current (DC) power source. The RF signal travels through the power divider into a lumped-element matching circuit ('L' type). The output signals of a four-way power divider (H4S-0.252WWP from Meca Electronics) with the same magnitude and phase are connected to SMA connectors attached on the wall using coaxial cables. A special four-way feeding network is acquired by exciting the front (+z) and back (-z) walls differentially as shown in Fig. 1 (b). The front (+z) copper plates are connected to the outer conductor of the SMA connector, while the copper plates on the back (-z) wall are

connected to the inner conductor of the SMA connector.

Full-wave numerical simulations are performed to assistant the design. Such electromagnetic simulations were performed using the commercial FDTD software SEMCAD X (ZMT, Zurich, Switzerland). Copper plates on the acrylic box are modeled as perfect electric conductor (PEC) on a dielectric box with a relative permittivity of 2.25 and an electrical conductivity of 0 S/m). The copper plates are modeled as ideal PEC with no thickness, the wall of the acrylic box is 12.5 mm thick, and the box outer dimensions are 300 mm by 300 mm by 120 mm. The SMA excitations are modeled as lumped sources, the gelled saline is modeled as a lossy dielectric material (relative permittivity = 78, electrical conductivity = 0.47S/m), the height of the gel is 90 mm, and the grid resolution of the simulation is 2.0 mm.

The matching circuit is modeled as lumped elements in series with the sources. Broadband simulations were performed to match the resonator at 64 MHz and 128 MHz for the 1.5T and 3T MRI systems. As shown in Fig. 2, we observed that the S_{11} values were below -10 dB, and the S_{21} values were below -15 dB. The numbering of the ports is shown in Fig. 1. The reflection and coupling of other ports are not shown since the structure is symmetric.

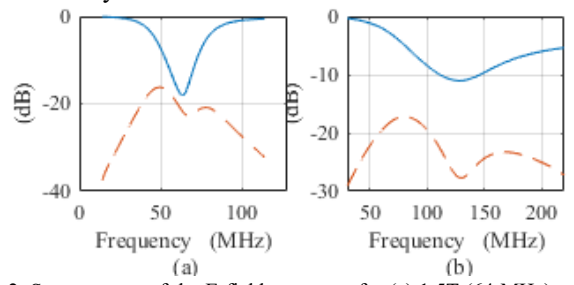


Fig. 2. S parameters of the E-field generator for (a) 1.5T (64 MHz) and (b) 3T (128 MHz). Blue solid line for S_{11} , red dotted line for S_{21} .

Based on the designed structure, electromagnetic simulations were performed for the two frequencies and the E-field distributions are shown in Fig. 3. The input power in the simulations are normalized to 32.52 W at 64MHz and 13.77 W at 128MHz respectively, so that the induced E-field in the generator will be equivalent to the E-field at the test in a standard ASTM phantom location (around111 V/m (64MHz) and 91 V/m (128MHz)) when the whole-body averaged phantom SAR is normalized to 2W/kg.

As shown in Fig. 3, for 1.5T (64 MHz), the E-field distribution is similar to that of a TE_{10} mode, whereas for 3T (128 MHz), the E-field distribution is similar to a combination of a TE_{10} and a TE_{21} modes. However, in both cases relatively uniform E-field distribution can be achieved in the center on the E-field generator.

The Q factor is assessed based on the stored energy and the consumed energy per period, the comparisons of the results and those from the analytical calculation are shown in Table 1. The main loss of the system is due to the power dissipation in the gel, the major contribution of the Q factor is from conductivity loss as:

$$Q_d = \frac{1}{\tan \delta} \tag{1}$$

$$\tan \delta \approx \frac{\sigma}{\omega * \varepsilon_0 \varepsilon_r}$$
 (2)

where σ is the electrical conductivity of phantom material ($\sigma = 0.47$ S/m), ω is the angular frequency ($\omega = 2 * \pi * 64$ MHz for 1.5T; $\omega = 2 * \pi * 128$ MHz for 3T), ε_0 is the vacuum permittivity, ε_r is the permittivity of the gel ($\varepsilon_r = 78$).

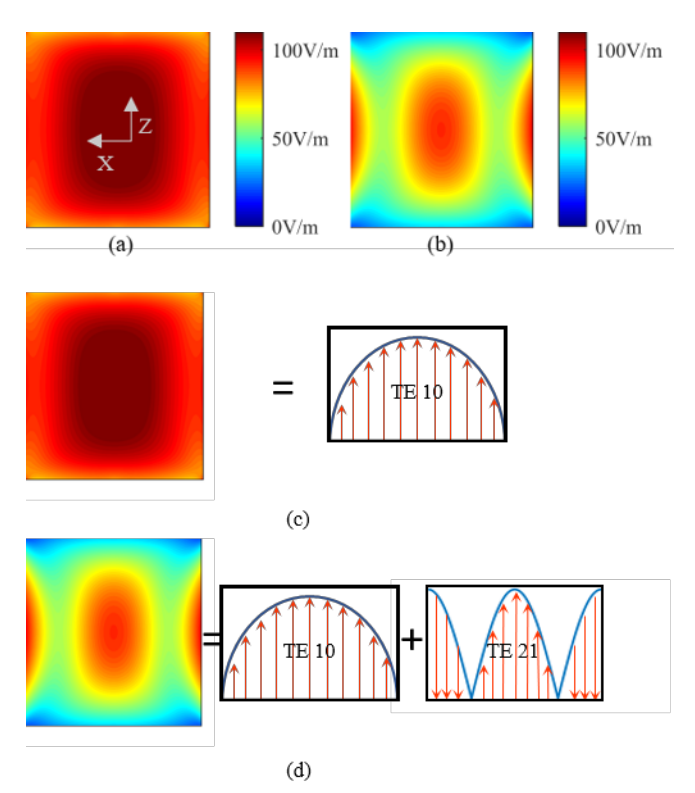


Fig. 3. Electric field distribution at the center slice of gel based on numerical simulation. (a) The electric field along the z-direction solved using the numerical method for 64 MHz. (b) The electric field along z-direction solved using the numerical method at 128 MHz. (c) single mode at 64MHz. (d) hybrid modes of 3T.

The Q factor (Q_s) can be obtained using:

$$Q_s = \frac{\omega_0' U}{P_d^{ave}} \tag{3}$$

where U is the stored energy, P_d^{ave} is the averaged power dissipated, and ω_0' is the real angular frequency.

TABLE 1. Q FACTORS COMPARISON

	Dielectric loss/W	Frequency /MHz	Stored energy/J	Q simu lation	Q _{theor} etical
64MHz	32.34	64	5.41e-8	0.67	0.61
128MHz	13.64	128	2.24e-8	1.32	1.17

B. Experimental validation of the design

To experimentally validate the E-field distributions inside the generator an E-field probe (Easy4MRI, ZMT, Zurich, Switzerland) was placed inside the generator at 49 locations (at the vertical center slice of the gel) as shown in Fig. 4. These 49 positions were chosen with a step size of 25 mm along the *x*-and *z*-direction. The E-field generator was filled with 90 mm gel and the E-field probe was placed 45 mm under the gel surface.

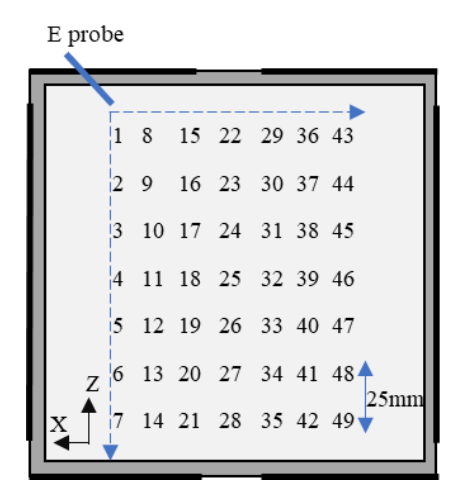


Fig. 4. Experimental validation of the E-field distribution using an E-field probe at different locations of the generator.

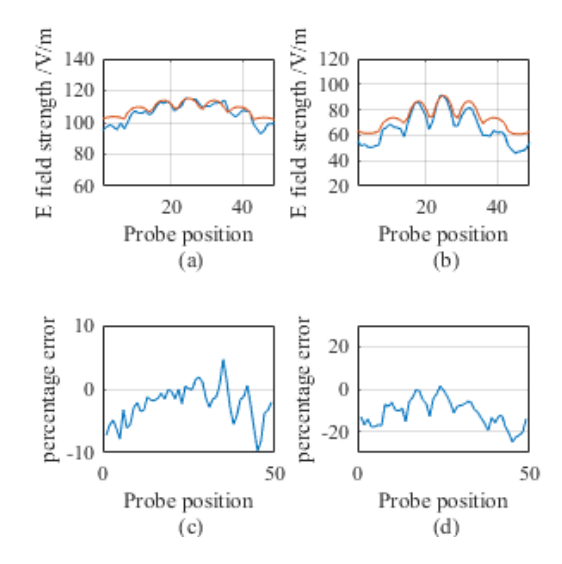


Fig. 5. Comparison of measured and calculated E-field inside the generator at 49 locations. (a) E-field at 64MHz, (b) E-field at 128MHz. The blue lines in (a) and (b) are the simulation and the red lines are the experimental results, (c) and (d) show the relative errors for 64MHz and 128MHz, respectively.

Comparisons of the E-fields obtained by direct measurement and simulation are shown in Fig. 5. All results shown here are for a net input power of 32.5W for 64MHz and 13.8W for 128MHz. Using this power levels, the E-field at the center of the generator will be similar to those at the ASTM recommended device testing location when a whole-body averaged phantom SAR of 2 W/kg is used. In the simulation the input power is calculated using the S parameter from the source sensors; the measurements are calibrated using the calorimetry method as suggested in [14][16]. As clearly shown in Fig. 4, the results obtained by experimental measurements were in good agreement with those from simulations for both the 1.5T (Fig. 3 (a)) and 3T (Fig. 3 (b)) systems. Such results validated our design.

C. Calibrations of the dual-frequency E-field generator

Two calibration procedures should be used to ensure the local E-field in the generator will be similar to those in the ASTM

phantom. The first calibration procedure is referred to as the input power calibration which follows the calorimetry procedure described in [14][16]. The second calibration procedure follows the procedure of local exposure estimation based on [14].

For the input power calibration we performed the following steps:

- 1. Fill the E-field generator with 90mm saline (not gelled) with a relative permittivity of 78, an electrical conductivity of 0.47S/m, and a weight of 6.85kg.
- 2. Cover the E-field generator with a thermal insulation lid to avoid evaporation and cooling of the saline which can produce a measurement error; leave the lid on the top of the E-field generator.
- 3. Measure the temperature at the center of the saline using a fiber probe until the temperature is stable (variation less than ± 0.5 °C).
- 4. Cover the entire system with thermal insulation material and apply the power for 900s.
- 5. Stop the power input, quickly stir the saline, measure the saline temperature rise with fiber probe.
- 6. Calculate the total deposited power in the saline using:

$$P = c * m * \frac{\Delta T}{\Delta t}$$

where c is the specific heating capacity of the saline, c = 4150 J/kg/K, m is the mass of the saline which is 6.85 kg, ΔT is the temperature rise of the saline, Δt is the heating time which is 900 s.

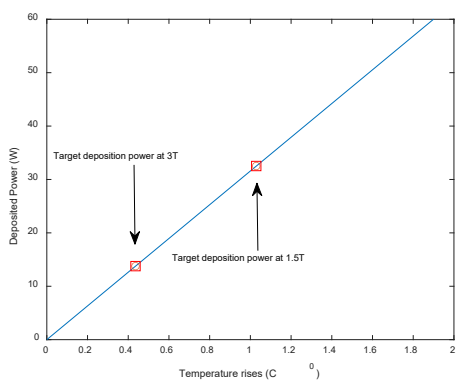


Fig.6. Calibration curve to estimate the input power based on calorimetry method.

Based on the procedure described above, one can generate the required power following the calibration curve as shown in Fig.6. As shown in the figure, the target deposition power inside the phantom should have corresponding temperature rises around 1.03 °C at 64MHz and 0.45 °C at 128MHz to generate an incident E-field of 111 V/m at 64MHz and 91 V/m at 128MHz.

In addition, a local exposure calibration should also be performed per [14] using a 3.2 mm x 10 cm titanium-alloy rod. Due to potential signal source drift and power amplifier variation between each experiment, the incident E-field at the center location of the generator can have slight variation. These variations should be captured through local exposure measurements. Therefore, before each device measurement, a

five-step local energy calibration procedure as described in [14] should be performed. In the test, the gelled saline should be used to fill the E-field generator to 90mm. Temperature rises for 6 minutes are measured near both ends of the titanium-alloy rod. The local SAR estimations (in terms of W/kg) should be estimated by $\Delta T_{360}/1.3$ at 64 MHz and $\Delta T_{360}/1.45$ at 128 MHz.

III. NUMERICAL STUDIES OF RF-INDUCED HEATING FOR IMDS

To show the equivalency of the RF-induced heating measurement between the E-field generator and the ASTM standard test system, two sets of IMDs were placed inside the E-field generator and the ASTM phantom (driven by an MRI RF coil). For the purpose of comparison, the 1g averaged specific absorption rate (SAR) was assessed [31]. During the RF-induced heating measurements in the E-field generator, the IMDs were placed at the center of the E-field generator, with the long axis of all devices aligned with the z direction.

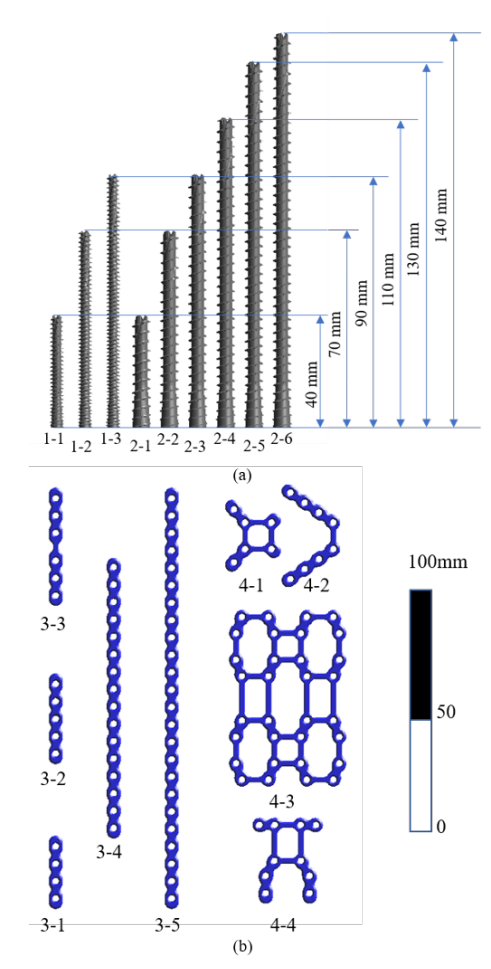


Fig.7. Simulation models of (a) standalone screws and (b) plate system family.

The two device families used in this investigation are shown in Fig.7. The first IMD family consists of fully threaded compression screws of different lengths and diameters. The second IMD family consists of plates and screws from a typical trauma product. Nine plates with different dimensions were loaded with different numbers of screws.

We studied the RF-induced heating of these devices when they were placed inside the E-field generator and the ASTM phantom. Both the E-field generator and the ASTM phantom were filled with 90 mm of gelled saline. During the RF-induced heating in the E-field generator, the devices were placed at the center of the E-field generator. In all studies using the ASTM phantom, the devices were placed at the center of *y*- and *z*-axis and 20 mm from the left (-*x*) edge of the ASTM phantom where a high electric field strength can be found [15]. In all the simulations, the IMDs are modeled as PECs, with a grid resolution of 0.5 mm.

In the RF-induced heating measurements using the ASTM phantom and an RF coil, the MRI RF coils were the MITS 1.5T system (ZMT, Zurich, Switzerland) and a standard commercial 3T RF coil. The dimensions of these coils are given in Table 2. In addition, two generic coil models were also used in the simulations. The simplified generic coils models were referred to as H8 coils [32]. They have hard current excitations on the legs of the coils. By varying the phase of those sources, the circular polarized (CP) mode can be generated. The dimensions of all physical and generic coils are shown in Table 2.

Table 2 DIMENSIONS OF THE COILS USED IN THE SIMULATION

	1.5T	3T	1.5T	3T
	Physical	Physical	Generic	Generic
Coil radius (mm)	350	305	315	315
Coil length (mm)	650	550	650	650
Shielding length (mm)	425	320	N/A	N/A
Shielding length (mm)	850	1450	N/A	N/A
Number of legs	16	16	8	8
Excitation type	IQ	IQ	Н8	Н8

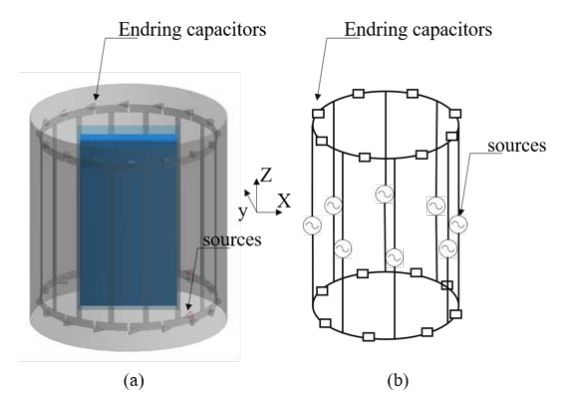


Fig.8. (a) Typical bird cage coil used for MRI scanning (b) simplified generic coil H8 (hybrid 8-port generic coil).

An illustration of those coils is shown in Fig.8 (a) and (b). The comparisons of simulation results for RF-induced energy near the devices is shown in Fig.9, and, all the SAR values

shown in the tables and figures were spatially averaged over a mass of one gram (1g). The input power of the ASTM system is normalized to a whole-body averaged SAR of 2 W/kg. Results obtained from the E-field generator were calibrated to the incident E-field at the device test location inside the ASTM phantom. As clearly shown in Fig.9, the E-field generator can produce similar energy deposition near the devices as those produced in the standard ASTM phantom.

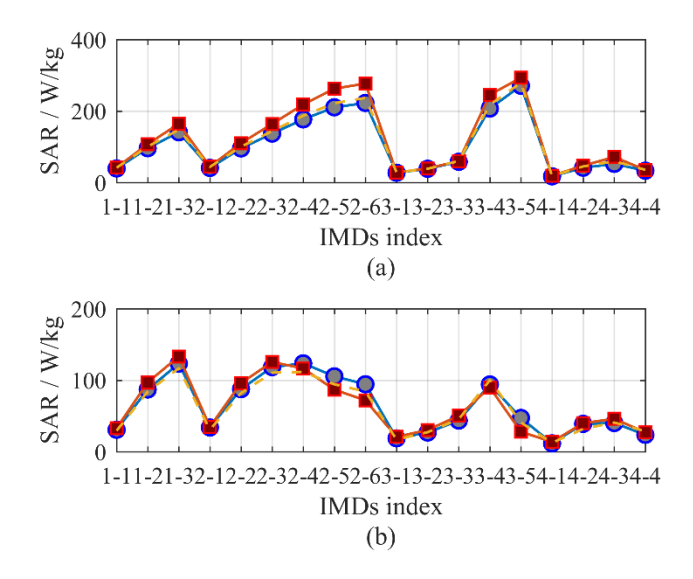


Fig.9. Comparison of 1g averaged SAR values in simulation for (a) screw family and plate system for the 1.5T MRI (64MHz), (b) screw family and plate system for the 3T MRI (128MHz), the blue solid line with the circles is for the ASTM standard test, red solid line with square is for the E-field generator, and the dashed is for the ASTM standard test.

A sensitivity analysis was then performed to understand the impact the device positioning error has on the energy deposition near the IMDs for both the ASTM method and the E-field generator. For the worst-case heating IMDs from each family, the IMDs are moved away from the center -10 mm, -5 mm, 5 mm and +10 mm along the x, y, and z axes. EM simulations were performed for the E-field generator and the ASTM phantom. Fig.10 shows the results for screw 2-6 at 64MHz and screw 1-3 at 128MHz. Fig.11 shows the results for plate 3-5 at 64MHz and plate 3-4 at 128MHz. As we can clearly see from these data, the newly designed E-field generator has similar sensitivity of the device positioning error along the z-direction as the ASTM phantom. However, the device positioning errors in the E-field generator along the xand y-directions are much smaller than in the ASTM phantom. Overall the E-field generator clearly outperforms the ASTM phantom in measurement uncertainty, power consumption, simplicity, size, and price.

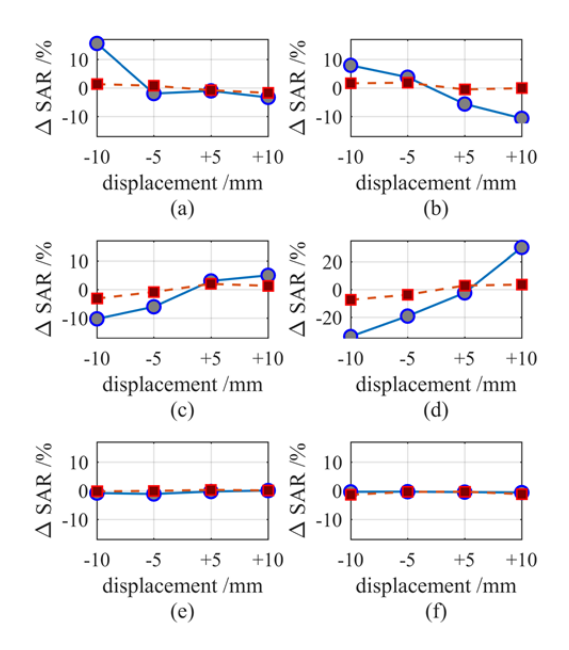


Fig.10. SAR sensitivity of the screw family with respect to positioning error along (a)(b) the \underline{x} -direction at 64MHZ and 128MHz, (c)(d) y-direction at 64MHz and 128MHz. The solid blue line indicates data in the ASTM phantom, while the dashed red line indicates data for the E-field generator.

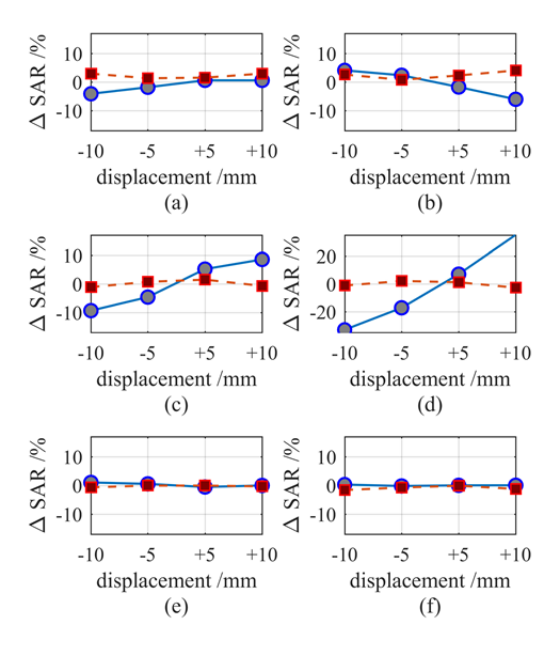


Fig.11. SAR sensitivity of the plates system with respect to positioning error along (a)(b) the x-direction at 64MHZ and 128MHz, (c)(d) y-direction at 64MHZ and 128MHz, (e)(f) z-direction at 64MHZ and 128MHz. The solid blue line indicates data in the ASTM phantom, while the dashed red line indicates data for the E-field generator.

IV. EXPERIMENTAL VALIDATION OF TEMPERATURE RISES

Based on the design presented above, a prototype of the E-field generator was developed as shown in Fig.12. IMDs were placed inside this test generator and the RF-induced heating was measured. In all measurements, the temperature probes were placed at the maximum heating location based on the

modeling results. For comparison, thermal simulations were also obtained using Pennes' bioheat based thermal solver in SEMCAD X. In both modeling and measurement, the RF power was turned on for 15 minutes. Temperature rises in both modeling and measurements are shown in Table III. All results are normalized a whole-body averaged SAR of 2W/kg for the ASTM phantom. For the E-field generator, the input power is chosen to generate an equivalent E-field. In both settings, the incident E-field at the device test location was 111 V/m 64MHz and 91 V/m at 128MHz.

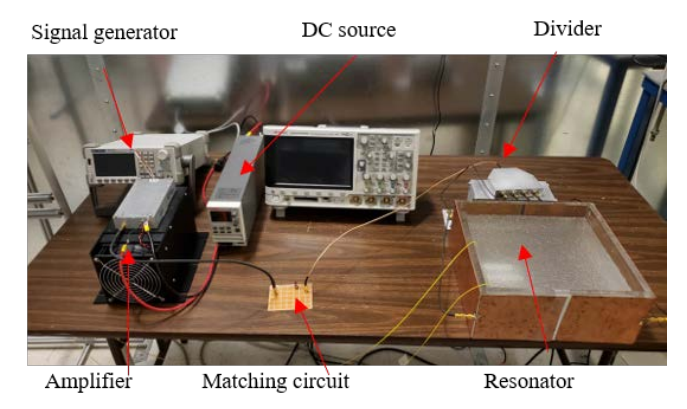


Fig.12.. Experimental setup for the E-field generator validation.

Table 3 Comparison of Measured and Simulated Temperature Rises for both $1.5 \mathrm{T}$ and $3 \mathrm{T}$

1.5T (64 MHz)	E-field generator			ASTM phantom		
Part Number	Modeli ng ΔT/°C	Measur ed ΔT/°C	Differen ce /%	Modeli ng ΔT/°C	Measur ed ΔT/°C	Differe nce /%
1-3	9.85	8.55	15.21	7.96	8.19	-2.76
2-4	11.96	11.13	7.48	9.38	9.34	0.48
2-6	15.36	15.22	0.91	11.8	10.79	9.37
3-4	14.08	13.01	8.23	11.8	10.10	16.86
3-5	16.68	15.24	9.41	15.3	12.60	21.42

3T (128 MHz)		E-field generator		ASTM phantom		
Part Number	Modeli ng ΔT/°C	Measur ed ΔT/°C	Differen ce /%	Modeli ng ΔT/°C	Measur ed ΔT/°C	Differen ce /%
1-3	7.76	6.73	15.29	7.22	7.86	-8.14
2-4	6.33	5.58	13.38	6.58	6.55	0.48
2-6	4.05	3.27	23.88	4.66	3.95	18.03
3-4	5.21	4.59	13.43	5.43	6.98	-22.19
3-5	1.82	1.70	7.06	2.97	2.60	14.23

As shown in Table 3, measured temperature rises are consistent with the results from simulations at both frequencies for both the E-field generator and the ASTM phantom. As shown in the table, relatively large errors were observed for devices longer than the ½ wavelength, which will be explained in the next section.

V. DISCUSSION

From the results presented in Fig.9 we can see that the induced SAR for most devices in the two IMD families at both 64MHz and 128MHz show a good agreement between the two different test systems. However, relatively large differences were observed for the longer devices 2-6, 3-4, and 3-5 at 64MHz as shown in the numerical simulations (Fig.9) and the experimental experiments (Table 3). Such relatively large differences are due to the E-field variations along the zdirection, as well as the potential interaction between the IMD and the E-field generator. In the ASTM phantom the E-field along the z-direction has a better uniformity than in the E-field generator since the E-field generator uses higher order modes. To achieve better agreement between the E-field generator and the ASTM phantom, the z-direction of the E-field generator can be extended which will lead to a better E-field uniformity. Currently, the RF-induced heating of the 10cm titanium rod is used to calibrate the local exposure. Using this calibration method, we find that for an IMD with a maximum length of less than 15 cm, the results obtained in the ASTM phantom and the E-field generator agree very well with each other. This agrees with the ASTM standard requirement that a 15 cm uniform incident E-field should be generated. Alternatively, one can develop better calibration parameters so that the averaged E-field along the z-direction is considered as a function of device length. Using this calibration a better agreement can be achieved. However, this is beyond the current calibration procedure described in the ASTM standard.

From the results shown in Fig.10 and Fig.11, we can see that the IMD positioning error along the z-direction would lead to negligible RF-induced heating differences. However, such differences can be magnified for positioning errors along the xand y-directions in the ASTM phantom. As clearly indicated in the figures, a positioning error of 5 mm along the x- or ydirection in the ASTM phantom, can change the induced SAR by 15%. Such variation can increase to 30% with a 10 mm positioning error along with these two directions. However, such a positioning error has almost no impact on the RFinduced heating when the E-field generator is used. The newly designed system can provide more consistent measurement results since the heating measurement is not very sensitive to the positioning error along all three directions. Based on these observations and a current side length of 30 cm, we observe that when the IMD overall length is less than ½ of the incident field wavelength, all results from measurement and modeling inside the ASTM phantom and the E-field generator agree well with each other.

Apart from the advantage of the measurement stability, the novel uniform E-field generator integrates both 1.5T and 3T testing into a single system without the need of an RF coil. In addition, using clinical, or clinically equivalent, MRI RF coils would require a large shielded room, a high-power amplifier, and a large footprint for the equipment. The novel uniform E-field generator has much smaller dimensions and requires less than 100W input power. This allows the E-field generator to become a desktop test system and an extremely useful alternative for IMDs MRI RF-induced heating measurements.

VI. CONCLUSION

In this paper we present a novel design of a uniform E-field generator. The design was guided by the cavity model and validated using numerical methods. Experimental validations of the design were performed by measuring the E-field distribution within the generator and compare it to simulation results. Two sets of IMD families were placed inside the Efield generator and the ASTM phantom for both modeling and measurement studies. From these studies, we observed highly correlated results for both frequencies 64MHz and 128MHz. In addition, the measured RF-induced heating is less sensitive to device positioning errors in the E-field generator. Compared to the conventional ASTM method using an RF coil and the ASTM phantom for testing, this novel E-field generator has a significant advantage in terms of low cost, low operation power, ease of operation, and most importantly, integration of 1.5T and 3T RF heating tests into a single desk-top system. This provides us with a better alternative to evaluate the RFinduced heating of IMDs under MRI exposure. It is observed that when the device length is less than ½ of the incident field wavelength, all results from measurement and modeling inside the ASTM phantom and the E-field generator agree within the combined uncertainty of 25%.

DISCLAIMER

The mention of commercial products, their sources, or their use in connection with material reported herein is not to be construed as either an actual or suggested endorsement of such products by the Department of Health and Human Services.

REFERENCES

- [1] J. Tian, D. Shrivastava, "In vivo radiofrequency heating in a 3T scanner," Theory and application of heating transfer in humans, vol. 2, Hoboken, NJ, USA: Wiley, 2018, pp. 621-630.
- [2] T. Kawamura, K. Saito, S. Kikuchi, M. Takahashi, and K. Ito, "Specific absorption rate measurement of birdcage coil for 3.0-T magnetic resonance imaging system employing thermographic method," *IEEE Trans. Microw. Theory Tech.*, vol. 57, no. 10, pp. 2508–2514, 2009.
- [3] J. Liu, J. Zheng, Q. Wang, W. Kainz, and J. Chen, "A Transmission Line Model for the Evaluation of MRI RF-Induced Fields on Active Implantable Medical Devices," *IEEE Trans. Microw. Theory Tech.*, vol. 66, no. 9, pp. 4271–4281, 2018.
- [4] S. Feng, R. Qiang, W. Kainz, and J. Chen, "A technique to evaluate MRI-induced electric fields at the ends of practical implanted lead," *IEEE Trans. Microw. Theory Tech.*, vol. 63, no. 1, pp. 305–313, 2015.
- [5] J. A. Nyenhuis, S. M. Park, R. Kamondetdacha, A. Amjad, F. G. Shellock, and A. R. Rezai, "MRI and implanted medical devices: Basic interactions with an emphasis on heating," *IEEE Trans. Device Mater. Reliab.*, vol. 5, no. 3, pp. 467–479, 2005.
- [6] J. A. Erlebacher, P. T. Cahill, F. Pannizzo, and R. J. R. Knowles, "Effect of magnetic resonance imaging on DDD pacemakers," *Am. J. Cardiol.*, vol. 57, no. 6, pp. 437–440, 1986.
- [7] A. M. Sawyer-Glover and F. G. Shellock, "Pre-MRI procedure screening: Recommendations and safety considerations for biomedical implants and devices," *J. Magn. Reson. Imaging*, vol. 12, no. 1, pp. 92– 106, 2000.
- [8] J. De Poorter, C. De Wagter, Y. De Deene, C. Thomsen, F. Ståhlberg, and E. Achten, "Noninvasive MRI thermometry with the proton resonance frequency (PRF) method: In vivo results in human muscle," *Magn. Reson. Med.*, vol. 33, no. 1, pp. 74–81, Jan. 1995.
- [9] P. Ehses et al., "MRI thermometry: Fast mapping of RF-induced heating along conductive wires," Magn. Reson. Med., vol. 60, no. 2, pp. 457– 461, 2008.

- [10] https://www.stryker.com/us/en/portfolios/neurotechnologyspine/neurovascular/embolization/test.html
- [11] https://www.jnjmedicaldevices.com/sites/default/files/user_uploaded_as sets/pdf assets/2019-09/MRI%20Safety%20Brochure.pdf
- [12] C. M. Collins et al., "Temperature and SAR Calculations for a Human Head Within Volume and Surface Coils at 64 and 300 MHz," J. Magn. Reson. Imaging, vol. 19, no. 5, pp. 650–656, 2004.
- [13] R. Yang, J. Zheng, W. Kainz, and J. Chen, "Numerical Investigations of MRI RF-Induced Heating for External Fixation Device in TEM and Birdcage Body Coils at 3 T," *IEEE Trans. Electromagn. Compat.*, vol. 60, no. 3, pp. 598–604, 2018.
- [14] ASTM F2182-19e. "Standard test method for measurement of radio frequency induced heating on or near passive implants during magnetic resonance imaging," 2019.
- [15] D. Li et al., "An Efficient Approach to Estimate MRI RF Field Induced in Vivo Heating for Small Medical Implants," *IEEE Trans. Electromagn. Compat.*, vol. 57, no. 4, pp. 643–650, 2015.
- [16] ASTM F2182-11a. "Standard test method for measurement of radio frequency induced heating on or near passive implants during magnetic resonance imaging," 2011.
- [17] Y. Liu, J. Chen, F. G. Shellock, and W. Kainz, "Computational and experimental studies of an orthopedic implant: MRI-related heating at 1.5-T/64-MHz and 3-T/128-MHz," *J. Magn. Reson. Imaging*, vol. 37, no. 2, pp. 491–497, 2013.
- [18] S. McCabe, J. Scott, and S. Member, "In the RF Field of MRI Scanners," vol. 65, no. 9, pp. 3541–3547, 2017.
- [19] S. M. Park et al., "Gelled Versus Nongelled Phantom Material for Measurement of MRI-Induced Temperature Increases with Bioimplants," *IEEE Trans. Magn.*, vol. 39, no. 5 II, pp. 3367–3371, 2003.
- [20] H. S. Ho, "Safety of metallic implants in magnetic resonance imaging," J. Magn. Reson. Imaging, vol. 14, no. 4, pp. 472–477, 2001.
- [21] F. G. Shellock, "Magnetic resonance safety update 2002: Implants and devices," J. Magn. Reson. Imaging, vol. 16, no. 5, pp. 485–496, 2002.
- [22] P. Nordbeck et al., "Measuring RF-induced currents inside implants: Impact of device configuration on MRI safety of cardiac pacemaker leads," Magn. Reson. Med., vol. 61, no. 3, pp. 570–578, 2009.
- [23] P. Nordbeck et al., "Spatial distribution of RF-induced E-fields and implant heating in MRI," Magn. Reson. Med., vol. 60, no. 2, pp. 312– 319, 2008.
- [24] Road vehicles Vehicle test methods for electrical disturbances from narrowband radiated electromagnetic energy, ISO Std. 11451-2, 2005.
- [25] V. Rodriguez, "Analysis of large E field generators in semi-anechoic chambers used for full vehicle immunity testing: Numerical and measured results," *IEEE Int. Symp. Electromagn. Compat.*, vol. 2014-December, pp. 681–684, 2014.
- [26] J. S. McLean, "Electric field generator incorporating a slow-wave structure," U.S. Patent 7.656.167, issued February 2, 2010.
- [27] C. Groh, J. P. Kärst, M. Koch, and H. Garbe, "TEM waveguides for EMC measurements," *IEEE Trans. Electromagn. Compat.*, vol. 41, no. 4 PART 2, pp. 440–445, 1999.
- [28] ISO/TS 10974:2018, 2nd Edition, "Assessment of the safety of magnetic resonance imaging for patients with an active implantable medical device," Apr. 2018.
- [29] H. F. Chen and K. H. Lin, "A numerical analysis of antenna factor of bilog antennas for normalized site attenuation and EMC measurement," *IEEE Int. Symp. Electromagn. Compat.*, vol. 2, pp. 817–821, 2003.
- [30] D. M. Pozar, "Microstrip antenna coupled to a microstrip-line," Electron. Lett., vol. 21, no. 2, pp. 49–50, Jan. 1985.
- [31] International Electrotechnical Commission (IEC), Medical electrical equipment - Part 2-33: Particular requirements for the basic safety and essential performance of magnetic resonance equipment for medical diagnosis (IEC-60601-2-33). IEC: Geneva, 2010.
- [32] E. Lucano et al., "Assessing the electromagnetic fields generated by a radiofrequency MRI body coil at 64 MHz: Defeaturing versus accuracy," *IEEE Trans. Biomed. Eng.*, vol. 63, no. 8, pp. 1591–1601, 2016.